IVYSPRING INTERNATIONAL PUBLISHER

Theranostics

2019; 9(2): 608-619. doi: 10.7150/thno.27952

Research Paper

Upconversion-Magnetic Carbon Sphere for Near Infrared Light-Triggered Bioimaging and Photothermal Therapy

Jiaxin Wang[1,2], Chenjie Yao[1], Bin Shen[1], Xiaohui Zhu[1], Yong Li[1], Liyi Shi[2], Yong Zhang[1], Jinliang Liu[1,2]✉, Yanli Wang[1]✉, Lining Sun[2,3]✉

1. School of Environmental and Chemical Engineering, Shanghai University, Shanghai, 200444, P. R. China
2. Research Center of Nano Science and Technology, Shanghai University, Shanghai, 200444, P. R. China
3. School of Material Science and Engineering, Shanghai University, Shanghai, 200444, P. R. China

✉ Corresponding authors: Jinliang Liu, PhD, School of Environmental and Chemical Engineering, and Research Center of Nano Science and Technology, Shanghai University, Shanghai, 200444, P. R. China. Email: liujl@shu.edu.cn. Yanli Wang, Professor, School of Environmental and Chemical Engineering, Shanghai University, Shanghai, 200444, P. R. China. Email: wangyanli@staff.shu.edu.cn. Lining Sun, Professor, Research Center of Nano Science and Technology, and School of Material Science and Engineering, Shanghai University, Shanghai, 200444, P. R. China. Email: lnsun@shu.edu.cn.

Received: 2018.06.18; Accepted: 2018.12.18; Published: 2019.01.21

Abstract

Nanoparticle-based theranostics combines tumor imaging and cancer therapy in one platform, but the synthesis of theranostic agents is impeded by chemical groups on the surface and the size and morphology of the components. Strategies to construct a multifunctional platform for bioimaging and photothermal therapy (PTT) are urgently needed. A new upconversion-magnetic agent (FeCUPs) based on hollow carbon spheres, which is both a photothermal agent and a dual carrier of luminescent and magnetic nanoparticles, provides an effective approach for tumor elimination.

Methods: The morphology of FeCUPs was characterized for the construction and size adjustment of the theranostic agent using transmission electron microscopy, high-resolution transmission electron microscopy, energy dispersive spectroscopy and high angle annular dark field scanning transmission electron microscopy. The distribution of FeCUPs was tracked under in-situ upconversion luminescence (UCL) imaging and magnetic resonance imaging (MRI) *in vivo*. Photothermal therapy was carried out on tumor-bearing mice, after which the toxicity of PTT was evaluated by a blood biochemistry test and histological section analysis.

Results: Stable and uniform loading of luminescent nanocomposites on three-dimensional carbon materials is reported for the first time. Based on the mechanism of synthesis, the size of the hybrid particles was adjusted from micrometers to nanometers. External magnetic field-enhanced photothermal therapy with multi-model imaging was accomplished using FeCUPs. Moreover, no cancer recurrence was found during 14 days of recovery without PTT.

Conclusions: Hollow carbon spheres, photothermal agents loaded with upconversion nanoparticles inside and magnetic nanoparticles outside were prepared for photothermal therapy. The aggregation of FeCUPs in tumors by the local magnetic field was verified by MRI and UCL imaging, and PTT was enhanced.

Key words: photothermal therapy, upconversion, magnetic, carbon, hollow

Introduction

Cancer is one of the most devastating diseases, causing more than 8 million deaths per year worldwide [1]. Under the urgent demand for cancer treatments, *in vivo* tracking techniques are a promising approach in imaging-assisted cancer therapy. Theranostics has emerged as an approach to

integrate imaging and therapy, generating research interest about nanoparticle-based nanoplatforms [2,3].

Currently, imaging is used in cancer therapy to monitor drug distribution. To ensure effective treatment of the tumor, imaging methods such as magnetic resonance imaging (MRI) and upconversion luminescence (UCL) imaging [4-6] have attracted considerable attention in recent years. Because of the strong contrast enhancement under external magnetic field, superparamagnetic iron oxide materials are used as T_2 contrast agents for MRI in tissue-level imaging [7] with high resolution [8]. Although MRI *in vivo* has no depth limit of detection, optical imaging methods have a higher resolution than MRI. UCL imaging utilizes the anti-stokes luminescence of upconversion nanoparticles (UCNPs) as detection source, which can avoid autofluorescence in tissue [9] and eliminate background noise dramatically. In addition, deeper tissue penetration can be achieved because its excitation and emission light wavelengths are both in the biological "optical window" (650-1000 nm) [10]. Under 980 nm near infrared (NIR) excitation, the 800 nm NIR emission caused by Tm^{3+}/Yb^{3+} doping is available [11-14], which makes NIR-to-NIR UCNPs a promising functional composite in the field of bioimaging.

Among cancer therapy techniques, photothermal therapy (PTT) is a phototherapeutic strategy that employs photothermal agents to convert light energy to thermal energy for non-invasive ablation of tumor cells [15,16]. PTT is not limited by tumor type [17]. Compared to magnetic hyperthermia therapy, which relies on alternating magnetic fields [18,19], PTT under laser irradiation is easy to operate and control. As a photothermal agent, carbon materials have many advantages: strong light absorbance in the UV-Vis-NIR region, extraordinary photothermal response [20,21], and a higher photothermal conversion efficiency than gold nanoparticles [22]. Among strategies to expand the performance of carbon materials, multifunction is realizable by shaping the carbonic structure. Notably, a hollow carbon sphere possesses a low density and a large cavity for storage and transportation of functional nanoparticles [23].

However, there are difficulties in integrating multi-functional nanoparticles on one nanoplatform due to the inherent limitations of each component, such as surface status, size, morphology and chemical composition. Here, we propose the use of a hollow carbon sphere that functions as a bridge to connect magnetic nanoparticles and luminescent nanoparticles and serves as an assembly medium for a multifunctional nanoplatform. Regarding the components of the nanoplatform, current approaches indicate that the integration of magnetic response and photothermal conversion improves the therapy effect in cancer [24,25] compared with single-function photothermal agents because the magnetic component enables convenient enrichment of the nanocomposites and magnetically targeted drug delivery [26,27].

In this case, a novel cancer theranostic agent was assembled by using a hollow carbon sphere to combine magnetic nanoparticles and UCNPs **(Scheme** 1). The new theranostic agent was fabricated with UCNPs loaded on the outer layer of the carbon surface and Fe_3O_4 in the cavity of the carbon sphere to minimize the light absorbance from Fe_3O_4 and the carbon layer. The size of the theranostic agents was adjusted from micrometers to nanometers to make it suitable for biological applications, and the formation mechanisms were discussed in detail. MRI-UCL dual-mode imaging and photothermal therapy for cancer were achieved in one nanoplatform and the PTT efficiency *in vivo* was improved under the treatment of an external magnetic field. To the best of our knowledge, this is the first report of the stable and uniform loading of UCNPs on carbon-based nanocomposites to realize near-infrared light-triggered bioimaging and photothermal therapy.

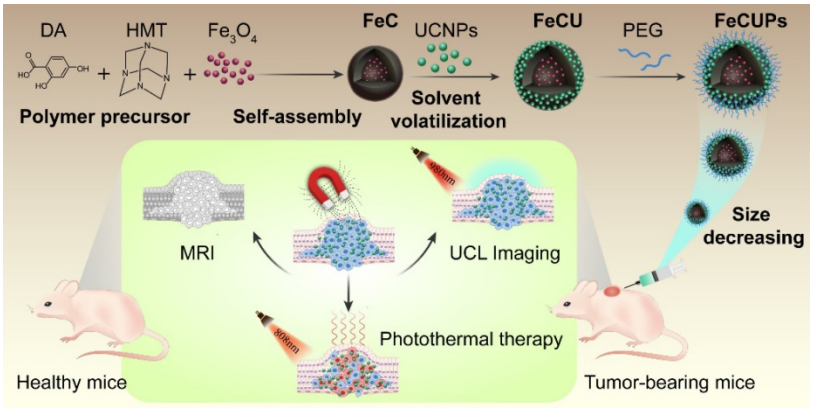

Scheme 1. Schematic illustration of the synthesis process of FeCUPs, and near-infrared light triggered bioimaging and photothermal therapy.

Results and discussion

Synthesis of the nanotheranostic agent and size adjustment

Using Fe(oleate)$_3$ as the precursor, Fe_3O_4 was synthesized via the pyrolytic process. Transmission electron microscope (TEM) images of the obtained Fe_3O_4 (Figure S1A) revealed a good monodispersed morphology in cyclohexane with an average diameter of approximately 6 nm. Two kinds of UCNPs (denoted UCNPs-Er and UCNPs-Tm) were synthesized via the solvothermal method. For UCNPs-Er, $NaGdF_4$:Yb^{3+},Er^{3+} nanoparticles were coated with an inert shell ($NaGdF_4$) to obtain core-shell structured $NaGdF_4$:Yb^{3+},Er^{3+}@$NaGdF_4$, which were both monodispersed in cyclohexane (Figures S1B and C). By changing the doped component from Er^{3+} ions to Tm^{3+} ions, $NaGdF_4$:Yb^{3+},Tm^{3+} and $NaGdF_4$:Yb^{3+}, Tm^{3+}@$NaGdF_4$ (UCNPs-Tm) were obtained with similar morphology to $NaGdF_4$:Yb^{3+},Er^{3+} and $NaGdF_4$:Yb^{3+}, Er^{3+}@$NaGdF_4$ (Figures S1D and E).

A sodium oleate (NaOA) micelle was formed on the surface of the Fe_3O_4, and a polymer precursor, which was synthesized with a one-step hydrothermal method, was assembled at the outer end of the NaOA micelle. After heat treatment (160 °C for 4 h), a hollow polymer structure was generated, which was named as FeP. FeP was transformed to FeC by a carbonization process (500 °C for 2 h). Notably, there were cracks in FeP but not in FeC, indicating that the mechanical strength was enhanced after carbonizetion (Figures S1F and G). The UCNPs were introduced by solvent volatilization and the FeCU nanocomposite was formed with UCNPs loaded on the outer layer and Fe_3O_4 in the cavity of the carbon sphere (Figure S1H). The selected area electron diffraction pattern of FeCU indicated that the UCNPs were in a hexagonal phase (Figure S1I). Through hydrophobic interaction [28], amphiphilic poly(ethylene glycol) (denoted PEG) was coated on FeCU for water-soluble modification to obtain the FeCUPs.

For biological applications, an appropriate particle size of the theranostic agent is critical [29,30]. It was supposed that the cavity size of the carbon sphere determined the size of FeCU, and the dimension of the spherical micelle of NaOA, which was first formed on the surface of the Fe_3O_4, determined the cavity size of the carbon sphere formed later. To reduce the particle size of FeCU and maintain the relatively large cavity for loading Fe_3O_4, adjustments in the NaOA concentration and other reactant ratios were made (Table S1). Generally, FeCU transformed from large nonuniformly shaped to smaller and more uniform particles (Figure 1A-C). For better dispersity in tumor tissue, the diameter of the FeCU was decreased and adjusted to approximately 216 nm (Figure 1C), and possessed a uniform and extended cavity with an average diameter of approximately 111 nm. The additive amount of Fe_3O_4 was increased and thus the cavity of the carbon sphere was filled with more Fe_3O_4 (Figure 1D). As shown in Figure 1E, the morphology of the FeCUPs was similar to that of FeCU after it was deposited for two months, and upconversion nanoparticles were also found on the surface of the FeC. Hence, the adherence of the UCNPs is relatively firm even under the influence of water-soluble modification and long-term storage.

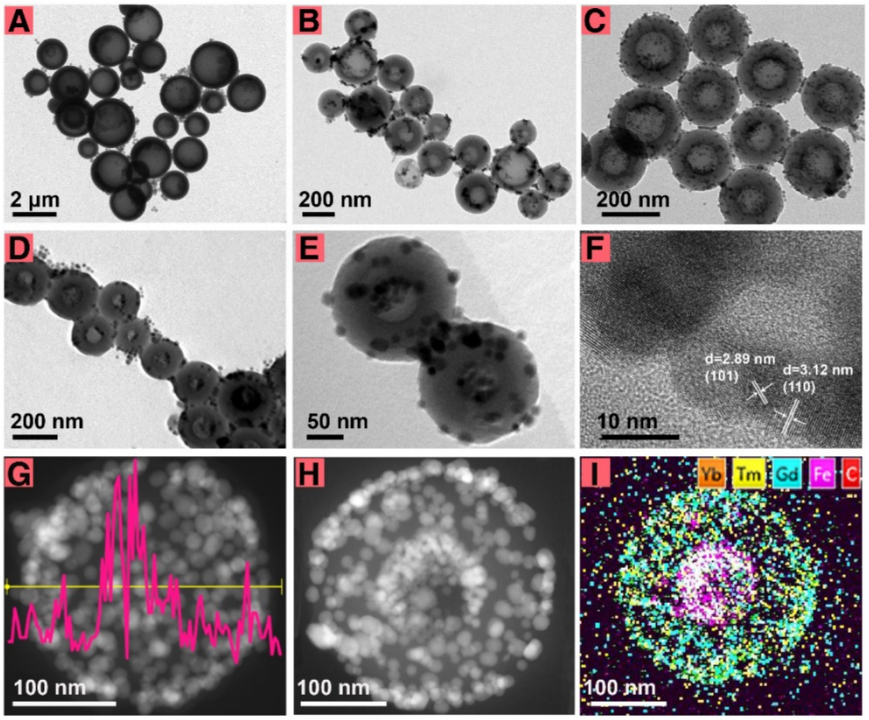

Figure 1. The morphology and structure characterization. TEM images of FeCU **(A-C)** with different diameters, **(D)** FeCU with more amount of loading Fe_3O_4. **(E)** TEM image of FeCUPs. **(F)** HRTEM of FeCU. **(G)** EDS line scan of Fe element in FeCU, and corresponding STEM-HAADF image. **(H)** STEM-HAADF image of FeCU and **(I)** corresponding element mapping of Yb (orange), Tm (yellow), Gd (blue), Fe (magenta), C (red).

To minimize the light absorbance from Fe_3O_4 and the carbon layer, UCNPs were coated on the outer surface of the carbon shell rather than in the cavity. The loading of UCNPs was impeded by many factors, including the morphology, size and surface

status of the UCNPs and FeC nanoparticles. Uniform loading of the UCNPs on FeC was unachievable when in rod-shaped (Figure S2A), comparatively large-sized (Figure S2B), without oleic acid ligands (Figure S2C), or with uneven particle size (Figure S2D). Furthermore, if the FeC was dispersed in water (Figure S2E), or the UCNPs were dispersed in chloroform (Figure S2F), the loading of UCNPs was not achievable. This is mainly because the excellent monodispersity of the FeC and UCNPs is a key factor for uniform loading. Second, ethanol and cyclohexane were used as dispersants to better facilitate the inter-diffusion of the FeC and UCNPs. When all dispersants were evaporated, the capillary pressure in the nanoscale [31-34] and interracial forces [35-37] drove the UCNPs to adhere to the FeC.

High-resolution transmission electron microscopy (HRTEM), energy dispersive spectroscopy (EDS) and high angle annular dark field scanning transmission electron microscopy (STEM-HAADF) were carried out to verify the synthesis of FeCU. As shown in Figure 1F, typical lattice fringes (d_{101} = 2.9 nm, d_{110} = 3.1 nm) of $NaGdF_4$ were found on the surface of the FeCU, indicating that $NaGdF_4$-based UCNPs existed on the carbon shell. Strong signal intensity peaks of the Fe element from EDS line scanning (Figure 1G) were positioned in the middle of FeCU. The STEM-HAADF image (Figure 1H) and element mapping of FeCU demonstrated the distribution of the UCNPs (Figure 1I). Based on the HAADF image of FeCU (Figure S3A) and corresponding element mapping images of the carbon (Figure S3B) and Fe (Figure S3C), the existence of the carbon cavity and loading of Fe_3O_4 were verified. Detailed data were collected to illustrate the combination between the UCNPs and the carbon shell. When the selected area (white square in Figure S3D) was magnified, typical lattice fringes (d_{110} = 3.07 nm, d_{102} = 1.87 nm) of UCNPs were observed (Figure S3E). The junction of the UCNPs and the carbon shell (white circle in Figure S3E) that was similar to the selected area in Figure S3F (white circle) showed transitions between regions with and without lattice fringes. Thus, it was suggested that the UCNPs and carbon shell combined closely via molecular diffusion.

The Fourier transform infrared (FTIR) spectra of PEG, UCNPs, FeCU, and FeCUPs (Figure S4) were analyzed to investigate the PEG modification of FeCU. The peak at 1563 cm^{-1} was attributed to the C=O stretching vibration of OA on the UCNPs (black line), this suggested the existence of UCNPs in the FeCUPs (blue line). Typical functional groups (N-C and C-O-C) of PEG were also observed in the FTIR spectra. Peaks at 1261 cm^{-1} and 1350 cm^{-1} were assigned to the N-C stretching vibration, and the peak at 1113 cm^{-1} was attributed to the C-O-C stretching vibration (red line), this proved the covering of amphiphilic PEG on the FeCUPs.

To demonstrate the surface status of the FeCUPs in different mediums for better therapeutic effect, the zeta-potential (ζ) and corresponding dynamic light scattering (DLS, d) were measured (Figure S5). It was suggested that the carboxyl group of PEG contributed to the negative ζ value of FeCUPs. For DLS, the existence of an electrolyte provided counter ions for the formation of an electrical double layer. Aggregation among particles decreased due to the repulsion from the electrical double layer [38]. Salt in medium increased the ionic strength, which compressed the thickness of the double layer and reduced the zeta potential [39]. Correspondingly, the diameter decreased. In addition, macromolecular proteins in DMEM (containing 10% fetal bovine serum (FBS)) absorbed on the FeCUPs via electrostatic force, which led to an increased diameter. Therefore, the diameter of the FeCUPs in saline was the smallest compared to other mediums.

Functional properties

As illustrated in Figure 2A, the T_2-weighted magnetic resonance signaling was reduced with increasing Fe concentration. The r_2 value was 845.13 mM^{-1} S^{-1}, which was much higher than that of magnetite nanoparticles published in previous reports [40-42]. Therefore, FeCUPs is a potential T_2 contrast agent. In addition, the hysteresis loops of FeC (Figure 2B) depicted that coercivity or remnant magnetization were not present, and the magnetization increases with magnetic field. As noted above, the magnetization was controllable because the cavity of the carbon sphere provided sufficient space for loading. When the added amount of Fe_3O_4 was doubled during the synthesis process (from 7.5 mg to 15 mg of Fe_3O_4), the resulting FeC possessed a saturation magnetization of 3.9 emu g^{-1}, which was 1.5-fold that of the FeC synthesized with less Fe_3O_4. When the layer of UCNPs was induced, the saturation magnetization was 3.6 emu g^{-1} (Figure S6). After further modification with PEG, the saturation magnetization decreased to 1.7 emu g^{-1} due to the coverage of nonmagnetic layers [43], random movement of Brownian motion [44], and the thermally blocked solid state of the FeCUPs. As shown in the inset in Figure 2B, FeC can be clustered on the side of the magnetic field, indicating that FeC has magnetization characteristics.

Given the UCL spectra of FeCUPs, the luminescent intensity was approximately 2.8 times higher as the concentration increased from 100 μg/mL to 400 μg/mL under 980 nm NIR laser

irradiation (Figure 2C). In addition, a similar trend of luminescent intensity increase was observed in the FeCUPs (UCNP-Er) system, and obvious luminescence was observable with 980 nm laser irradiation at 1.5 W/cm² (Figure S7).

The luminescent stability of FeCUPs was studied to illustrate the stability of the UCNPs adhesion. No obvious change of luminescent intensity at 800 nm was observed with continuous irradiation of a 980-nm NIR laser (455 mW cm^{-2}) for 70 min (Figure S8A and B). After one week of storage, the luminescent intensity was stable regardless of whether the sample was dispersed in water (Figure S8C) or saline (Figure S8D). After being stored in water for one week, the supernatant and pellet of FeCUPs (400 μg/mL) were collected after centrifugation (5000 rpm, 10 min). Under irradiation with a 980-nm NIR laser (1.5 W cm^{-2}), no obvious luminescence was observed in the supernatant. Thus, it was suggested that the FeCUPs possessed luminescent stability and there was relatively tight adhesion of the UCNPs.

As a prerequisite to realize photothermal conversion, the light absorbance ability is significant for synthesized materials. In the absorbance spectra (Figure 2D), a strong absorbance was observed in the visible-to-NIR region. Considering light penetrability in an organism, we used an 808-nm NIR laser as the excitation light source. The trend of temperature variation was observed via infrared thermography camera. The temperature obviously increased with higher concentrations and longer irradiation times (Figure S9A). The photothermal conversion curves were measured using a microthermocouple upon 808 nm laser treatment (1.5 W/cm²). As shown in Figure 2E, the temperature increased obviously until reached a plateau after 300 s of continuous irradiation with the 808 nm laser. If laser irradiation was stopped, the temperature decreased (Figure S9B left). Furthermore, the photothermal conversion efficiency of the FeCUPs (400 μg/mL) was calculated as 47.4% using a previous method (Figure S9B right) [45,46], which was higher than most current photothermal carbon material agents [47,48].

Cytotoxicity

The cytotoxicity of the FeCUPs nanoparticles in HeLa and GES-1 cell lines were explored. As shown in Figures S10 and S11, the cell viabilities exceed 95% when the concentration of nanoparticles varied from 25 μg/mL to 500 μg/mL with a 24-h incubation time. Only a slight decline of the viabilities of GES-1 was observed after 48 h incubation (Figure S11). These results demonstrate that the FeCUPs nanoparticles possessed good biocompatibility. Next, the effect of PTT *in vitro* was studied by changing the experimental conditions such as with/without irradiation and changing the concentration of nanoparticles. The results indicated that the cell viability was above 99% when treated with NIR alone, which indicated that the heating effect of the laser to the cells was limited. As expected, the cell viabilities decreased rapidly with incubation of the nanoparticles and 808 nm irradiation. In addition, a higher concentration led to a better photothermal conversion effect and thus lower cell viability. Therefore, it was believed that the nanoparticles and the laser itself do not effectively lead to cell death except when FeCUPs was

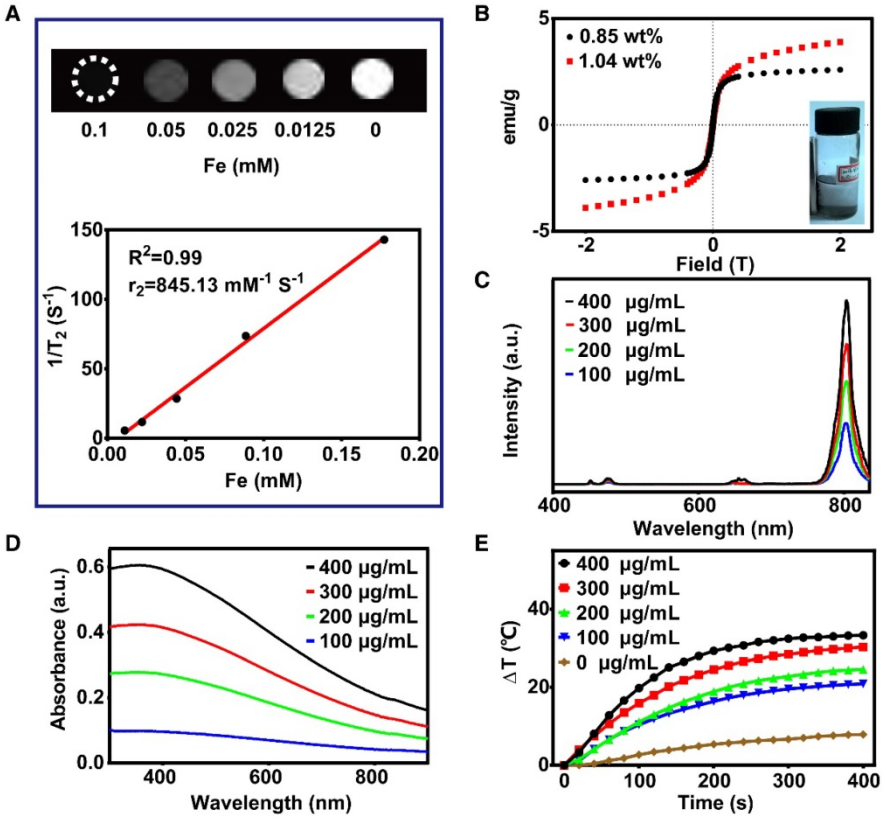

Figure 2. Functional properties analysis. (A) T_2-weighted MRI of FeCUPs **(A, upper)**; linear fitting with $1/T_2$ and Fe concentration of FeCUPs **(A, bottom)**. **(B)** Hysteresis loops of FeC loaded with different amount of Fe_3O_4, and Fe contents are 1.04wt% and 0.85wt% respectively (insect: FeC was attracted by a magnet). **(C)** Upconversion emission spectra of FeCUPs, UCNPs: $NaGdF_4$:Yb^{3+},Tm^{3+}@$NaGdF_4$, **(D)** UV-Vis-NIR absorption spectra, and **(E)** Photo-thermal conversion curves of FeCUPs (808nm, 1.5W/cm², UCNPs: $NaGdF_4$:Yb^{3+},Tm^{3+}@$NaGdF_4$).

used as a photothermal converter and treated with an 808-nm laser (1.5 W/cm^2).

Multi-model imaging *in vivo*

The multi-model imaging of FeCUPs was administered to subcutaneous tumor models in which HeLa cells were implanted in the root segment of the right forelimb. When the tumors grew large enough (> 0.5 cm^3) and became stiff, multi-model imaging applications were implemented *in vivo*. First, in the T_2-weighted MRI image, a signal decline in the selected area (dark circle) before/after the injection was apparent using FeCUPs. Without a magnetic field (NO MF group) (Figure S12A), the intensity decreased from 213.0 ± 28.9 a.u. to 188.5 ± 33.2 a.u. and the average decline rate was 11.5%; in the magnetic field (MF group) (Figure S12B), the intensity decreased from 217.0 ± 28 a.u. to 190.0 ± 24.5 a.u. and the average decline rate was 12.4%. The peak signal intensity in the selected circle changed significantly only in the MF group with a decline rate of 54%. Therefore, the accumulation of FeCUPs at the tumor site was enhanced by magnetism.

The UCL imaging *in vivo* (upper of Figure 3C) was studied by using one tumor-bearing mouse injected with nanoparticles (4 mg/mL) *in situ*. After 1.5 h, apparent intensity variation was observed at the tumor region. After 3 h, the UCL intensity decreased relatively. In addition, intensive luminescence was observed in the collected tumor slice under a confocal microscope with 980-nm NIR laser irradiation. (bottom of Figure 3C). It can be deduced that FeCUPs spread across the subcutaneous tumor tissue. For photothermal imaging, as shown in Figure 3D, the temperature was enhanced at the local magnetic field-treated tumor site, indicating that magnetic attraction improved the local concentration of FeCUPs.

PTT in vivo

Considering the efficient photothermal conversion effect of the FeCUPs, further experiments based on five groups of subcutaneous tumor-bearing mice were conducted to test the possibility of oncotherapy. The saline group was set as the blank group. The NIR group and material group were set as the conditional groups. The remaining two groups were PTT groups with and without magnetic treatment. In terms of the tumor volume variation trend (Figure 4A), the conditional groups showed no tumor inhibition impact, and thus the tumor continued to grow as in the blank group. After 808-nm laser irradiation (14 days) and 14 days of recovery, the physiological features of mice in the PTT groups were similar to those of the normal group.

Regional magnetic field treatment was critical to obtain a better therapeutic effect. For inhibition of tumor growth, the tumor volume in the PTT groups started to decrease after 10 days of laser treatment. The tumors in the +NIR group were eliminated on the 18th day, and disappeared in the +NIR+MF group on the 16th day. During the 14-day recovery, it was observed that only mice in the +NIR+MF group could move freely and were as active as the mice in the normal group. Mice in the +NIR group could move freely, but were not as active as those in the +NIR+MF group. Mice in the NIR, material and saline groups whose movement were impeded by their tumors were observed

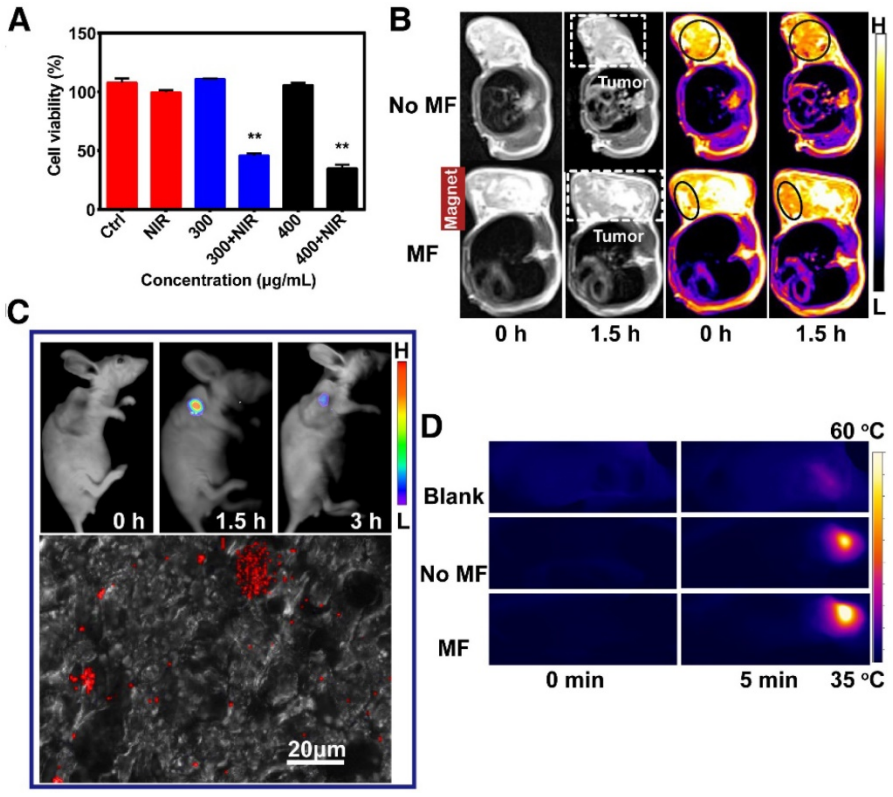

Figure 3. Cytotoxicity *in vitro* and imaging *in vivo*. (A) Cell viabilities of HeLa cell s incubated in different conditions: control, NIR, 300 μg/L material, 300 μg/L material + NIR, 400 μg/L material, 400 μg/L material + NIR, (** = p<0.01, compared with control group, one-way ANOVA). **(B)** T_2-weighted MRI of mice treated with magnet and corresponding pseudo-color images. Dark circle referred to the selected area with signal decline in tumor after the injection by using FeCUPs. **(C)** UCL imaging of mice (upper) and CLSM image of tumor slice (bottom) under 980 nm laser irradiation. **(D)** Thermal images of mice under 808 nm laser irradiation.

every other day and appeared to gather together. These phenomenon help illustrate the enhanced PTT efficacy with magnetic treatment.

At the end of the recovery period, photos of excised tumors (Figure 4B) exhibited that tumors in the +NIR+MF group were much smaller than those in the +NIR group, except for disappeared tumors that the empty positions referred to. Moreover, the statistical results of excised tumors (Figure 4C) clearly illustrate differences among the 5 groups. For the NIR and material groups, the tumor volume was similar to that of the saline group, which implied that the tumor had been growing until the mice were sacrificed. However, there was a significant decline of tumor volume in the +NIR and +NIR+MF groups, which means PTT resulted in an effective therapeutic effect. Moreover, the tumors almost disappeared with extra magnetic treatment, a lower dosage was used due to magnetic enrichment (Inset of Figure 4C), and particles with large size enhanced retention.

In addition, the distribution of the Fe element in heart, liver, spleen, lung, and kidney tumors was investigated by inductively coupled plasma-atomic emission spectrometry (ICP-AES), which could illustrate the magnetic enrichment (Figure S13). Under magnetic treatment, the retention of FeCUPs at the tumor site was enhanced. In the +NIR group, the average Fe element in tumors was 106.77 mg but increased to 217.27 mg in the +NIR+MF group, 2-fold higher than the +NIR group (n=3). Additionally, the FeCUPs spread in the organs of mice increased. It was suggested that a small portion of the FeCUPs was transported to internal organs via body fluid, except for the FeCUPs that was removed during ablation and recovery of the tumor. Due to the magnetic field-induced increment in dose and the relatively large particle size [49], the distribution of FeCUPs was higher in the reticuloendothelial system (liver, spleen, lung), especially for the liver in +NIR+MF.

To evaluate the health condition of the mice, body weights were recorded every other day during the therapy (Figure 4D) and barely fluctuated in all groups. Therefore, FeCUPs or NIR treatment did not have a significant side effect on body growth. For toxicity evaluation *in vivo*, blood serum samples of all groups were examined after the PTT treatment. Three tumor biomarkers (CEA, AFP, CA50) were studied to analyze the degree of malignancy because they represent the gene expression degree of related tumor cells and responses of other body parts during tumor growth [50]. As Figure 4E implies, laser-induced thermal ablation in PTT groups affected tumor promotion compared to the saline group. Furthermore, the degree of malignancy was analyzed histologically (Figure S14). The tumor slices showed that the necrotic rate in the +NIR+MF group was the lowest. Thus, magnetic treatment enhanced the therapeutic effect compared to the +NIR and saline groups.

In addition, hepatic and renal function (Figure S15) were investigated. Both urea and serum creatinine (CREA) values were in normal ranges. The important hepatic indicators, alanine aminotransferase (ALT) and aspartate aminotransferase (AST), showed no significant changes. In the material and PTT groups, there was a slight decline in total bilirubin (TBIL). The decline in TBIL was suggested to be related to the interference of injected FeCUPs with blood transportation. Although the alkaline phosphatase (ALP) showed an increase in the material group through metabolism, suggesting that a small portion of injected FeCUPs was transported to internal organs, minor liver injury might have occurred in the material group, which corresponds to the observed distribution of the Fe element. Notably, ALP recovered to a normal value in the PTT groups. The injected FeCUPs was supposed to be mainly positioned in the tumor and removed with elimination of the tumor. Consequently, the functions of the liver and other inner organs in the PTT groups tended to be better than those of other groups.

Statistical analysis of six parameters (CREA, ALT, AST, TBIL, ALP) indicated that the kidney and liver functions of mice in the PTT groups remained normal. No obvious inflammation was observed in the PTT groups through analysis of histological features examined by H&E staining of organ slices, including the heart, liver, spleen, and kidneys (Figure S16).

Conclusions

In summary, FeCUPs based on a hollow carbon sphere that acted as a cheap and strong base for photothermal conversion and carrier of Fe_3O_4 and UCNPs were fabricated step-by-step. The UCNPs were first coated on the carbon sphere by solvent volatilization for the photothermal agent. The size of the theranostic agent was optimized according to the synthesis mechanism for therapeutic enhancement. The PTT effect of FeCUPs *in vitro* and *in vivo* was studied. In the presence of a magnetic field, the aggregation of FeCUPs in tumors was verified by MRI and UCL imaging, and PTT was enhanced. The tumor was eliminated by laser irradiation with no recurrence in 14 days. We envision that future works could focus on loading other nanomaterials inside and outside the hollow carbon sphere to explore applications in energy conversion, information transmission, and catalysis.

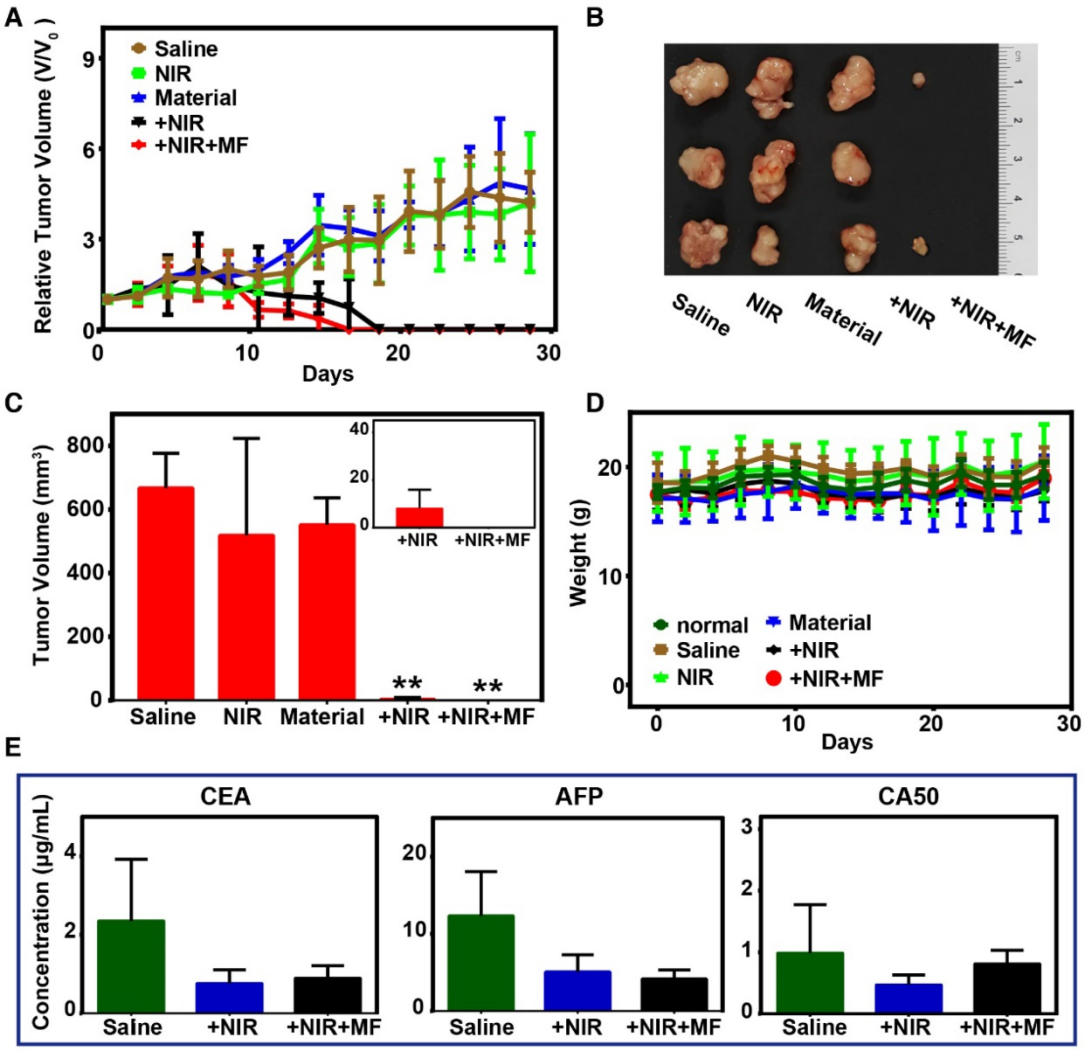

Figure 4. Photo-thermal therapy and evaluation *in vivo*. (A) Tumor growth curves of different groups. **(B)** Photographs of excised tumors in each group after 28 days. **(C)** Volume of excised tumors (** = p<0.01, compared with saline group). Inset: the tumor volume of +NIR and +NIR+MF groups with minimized range of Y axis. **(D)** Body weights variation trend. **(E)** Tumor biomarkers results from blood serum biochemistry.

Methods

Materials

All of the chemicals in this report were used without any further purification. Hexamethylene-tetranrine (HMT, AR), dichloromethane (CH_2Cl_2, AR), anhydrous ethanol (AR), acetone (AR), cyclohexane (AR), iron (III) chloride hexaydrate (AR) were obtained from Sinopharm Chemical Reagent Co. China. Oleic acid (OA), 1-octadecene (ODE), poly (maleic anhydride-alt-1-octadecene) (number-average molecular weight (M_n) =30-50 kDa, powder), yttrium (III) chloride hexahydrate ($YCl_3 \cdot 6H_2O$), ytterbium (III) chloride hexahydrate ($YbCl_3 \cdot 6H_2O$), erbium (III) chloride hexahydrate ($ErCl_3 \cdot 6H_2O$), gadolinium (III) chloride hexahydrate ($GdCl_3 \cdot 6H_2O$) were obtained from Sigma-Aldrich Co. Ltd. Sodium oleate (CP), methanol (GC), n-hexane (AR), triethylamine (TEA, AR), ammonium fluoride (GR), sodium hydroxide (GR), N-hydroxysuccinimide, N-(3-dimethylamino-propyl)-N′-ethylcarbodiimide hydrochloride, 2,4-di-hydroxybenzoic acid (DA), and methoxypolyethylene glycol amine (Mn = 2 kDa) were obtained from Shanghai Aladdin Chemistry Co., Ltd (Shanghai, China).

Synthesis of Fe_3O_4

Fe_3O_4 nanoparticles were synthesized using the procedures described in ref. [51]. The obtained nanocrystals were dissolved in n-hexane (30 mg/mL) and sealed for storage.

Synthesis of UCNPs

First, a $GdCl_3 \cdot 6H_2O$ solution (1 M, 3180.0 μL), $YbCl_3 \cdot 6H_2O$ solution (1 M, 800.0 μL), and $TmCl_3 \cdot 6H_2O$ solution (0.1 M, 200.0 μL) were mixed and heated to 110 °C. Oleic acid (22.0 mL, 130 °C, 30 min) and 1-octadecene (18.0 mL, 130 °C, 30 min) were then added. Next, a methanol solution (20.0 mL) of NaOH

(640.0 mg) and NH_4F (948.4 g) was added. After stirring for one night, the methanol was evaporated at 60 °C under vacuum, then heated to 110 °C for 30 minutes and maintained at 300 °C for 1 h in flowing argon. Acetone and cyclohexane were used to collect the UCNPs. The core was reserved in cyclohexane (20.0 mL).

Second, a $GdCl_3 \cdot 6H_2O$ solution (1 M, 800.0 μL) was heated to 110 °C. Oleic acid (22.0 mL, 130 °C) and1-octadecene (18.0 mL, 130 °C) were added and the solution was cooled to 50 °C. The prepared core was added and heated to 60 °C under vacuum. A methanol solution (10.0 mL) of NaOH (67.4 mg) and NH_4F (37.1 mg) was added and heated to 60 °C under vacuum. The following steps were similar to synthesis of the core described above. The final product (UCNPs-Tm) was stored in cyclohexane (10.0 mL). The synthesis process of UCNPs doped with Er (UCNPs-Er) was similar to that of UCNPs-Tm.

Synthesis of FeC

FeC was synthesized according to the methods reported in ref. [52] with a few modifications. Sodium oleate (NaOA), the surfactant and soft template were used to convert oleate-capped Fe_3O_4 into an aqueous phase. DA and HMT acted as the precursor of the polymer layer. NaOA (10 mg) was first dissolved in deionized water (3 mL). Then, Fe_3O_4 (50 μL) was added. The solution was dried (50 °C, 4 h) and mixed with a water solution (47.5 mL, 85-90 °C) of DA (0.0771 g, 98%) and HMT (0.0175 g). The mixture was reacted at 160 °C for 4 h. The solid was collected by centrifugation (8000 rpm, 10 min) and transferred to FeC under 500 °C for 2 h (H_2/Ar = 5%/95%).

Solvent volatilization synthesis of FeCU

FeC (2.0 mg) was dispersed in ethanol (6.0 mL) and stirred for 12 h. The prepared UCNPs-Tm solution (1.0 mL) was diluted with cyclohexane (5.0 mL). The FeC dispersion was added slowly to this solution and stirred for 30 min. It was then heated to 60 °C to evaporate the solvent, and the resulting viscous solution was dissolved in cyclohexane (20.0 mL). The solid product was collected via centrifugation (8000 rpm, 10 min). The solid product was washed with cyclohexane 3 times before collecting the FeCU.

Synthesis of FeCUPs

Amphiphilic poly(ethylene glycol) was synthesized according to previous literature [53,54]. The loading process was enlightened by a relevant report [55]. FeCU (1.0 mL) was diluted with cyclohexane (4.0 mL), which was then added into a chloroform solution (5.0 mL) of amphiphilic poly(ethylene glycol) (50.0 mg). The resulting mixture was heated to 60 °C and a viscous solution formed. Deionized water (15.0 mL) was added while stirring. After centrifugation (5000 rpm, 10 min), the FeCUPs was gathered, dispersed in deionized water (1.0 mL), and stored at 4 °C.

Characterization

Morphologies were observed by TEM (JEM-200CX, JEOL) and HRTEM (JEM-2010F, JEOL). FTIR spectra were obtained by FTIR spectroscopy (AVATAR370, Nicolet). Fluorescent spectra were investigated by fluorescent spectroscope (FLS920; Edinburgh) and the absorption spectra were investigated by UV-VIS Spectrophotometer (UV-2600; SHIMADZU). The element content was analyzed by ICP-AES (7300DV; PERKINE).

Cell culture and animals

HeLa cells (human cervical carcinoma cell line) were obtained from the Chinese Academy of Sciences. GES-1 (gastric epithelial cell line) were obtained from Nanjin Cobioer Biotechnology Co., Ltd. Dulbecco's modified Eagle's medium (DMEM) and fetal bovine serum (FBS) were obtained from Gino Biological Pharmaceutical Technology co., Ltd (Hangzhou, China). Cells were maintained in appropriate culture medium supplemented with 10% FBS and incubated at 37 °C in a 5% CO_2 atmosphere.

Female Balb/c nude mice (4-6 weeks age, subcutaneous tumor transplanted onto shoulder using Hela cells) and healthy female Balb/c nude mice were obtained from Beijing Vital River Laboratory Animal Technology Co., Ltd. All the animal experiments were operated in compliance with the criteria of the National Regulation of China for Care and Use of Laboratory Animals.

Toxicity evaluation *in vitro*

FeCUPs was dispersed in PBS (pH 7.4) to a concentration of 30 mg/mL. The cytotoxicity of the FeCUPs nanoparticles was evaluated using the HeLa cell line. The cell viability was expressed as the percentage of viable cells of the total cells. HeLa cells seeded in 96-well plates (5×10^3 cells per well) were incubated in DMEM culture medium containing different concentrations (0, 25, 50, 100, 150, 200, 300, 400 and 500 μg/mL) of FeCUPs nanoparticles for 24 and 48 h. The cell viability of each well was measured with a CCK-8 Kit (Dojindo Laboratories, Japan). To evaluate the cytotoxicity of FeCUPs nanoparticles to normal cells, the GES-1 cell line was selected and tested following the same procedures as for the Hela cell line.

In addition, the cytotoxicity of FeCUPs nanoparticles after laser treatment was also evaluated. HeLa cells were co-incubated with 300 and 400

μg/mL nanoparticles for 24 h, followed by continuous wave (CW) diode laser irradiation at 808 nm and 1.5 W for 5 min (K808F02mn - 8.000W; BWT BEIJING) with a facula diameter of ~6.5 mm and were incubated at 37 °C for another 24 h before detection. Cells irradiated under the same condition but without incubation of nanoparticles were chosen as the control. Cells incubated with 300 and 400 μg/mL nanoparticles but without laser treatment were also used as a control.

UCL imaging *in vivo*

A saline solution of FeCUPs (4 mg/mL) was injected intratumorally into tumor-bearing mice. After 1.5 h, a UCL image was captured using an in-vivo imaging system (NightOwl II LB 983; Bernold Technologies GmbH & Co. KG, Germany) at λ_{ex} = 980 nm and λ_{em} = 800 nm.

Magnetism of the material and T_2-weighted MRI *in vitro* and *in vivo*

The magnetism measurement was performed using a Vibrating Sample Magnetometer (7407; lakeshore) at room temperature. The MRI property was measured using a 3T MR scanner (MAGNETOM Trio Tim; SIMENS). The r_2 relaxivity was obtained by linear fitting of the $1/T_2$ relaxation time (s^{-1}) versus the Fe^{3+} concentration (mM). For the MRI *in vivo* imaging, a saline solution of FeCUPs (2 mg/kg) was injected intratumorally into tumor-bearing mice and the magnet was fixed near the tumor site. MR scans were taken before and 1.5 h after the injection. Mice received intraperitoneal anesthesia (0.1 mL/10 g, 10% chloral hydrate) during the experiment.

Photothermal conversion and imaging *in vitro* and *in vivo*

Gradient concentrations of FeCUPs (solid content: 0, 100, 200, 300, 400 μg/mL) were treated with an 808-nm NIR laser (1.5 W/cm^2), and the temperature was measured using a microthermo-couple (GM1312; BENETECH) and monitored using an infrared thermal imager (PI400; optris). The irradiation time was also recorded. A saline solution of FeCUPs (4 mg/mL) was injected intratumorally into tumor-bearing mice; after 4 h, thermal images and the irradiation time were recorded (808 nm at 800 mW/cm^2).

PTT, toxicity and histology analysis *in vivo*

Further experiments were based on five groups of subcutaneous tumor-bearing mice to evaluate the possibility of oncotherapy. HeLa cells were implanted at the end of the right forelimb. When the tumors grew large enough (> 0.5 cm^3) and became stiff, further *in vivo* applications were studied. Three healthy Balb/c nude mice were used as the normal group. The tumor-bearing mice were randomly divided into 5 groups (n = 3, per group), the saline (100 μL) group, NIR group (808 nm, 10 min, 800 mW/cm^2), material group (saline solution of FeCUPs, 2 mg/kg), +NIR group (808 nm, 10 min, 800 mW/cm^2; saline solution of FeCUPs, 2 mg/kg), and +NIR+MF group (+NIR group with magnetic field (MF)). All tumor-bearing mice were injected *in situ*. The tumor volume was measured by Vernier caliper and the body weight was measured by electronic balance every other day. The tumor volume was calculated using the following equation: tumor volume = width^2 × length/2. 808-nm NIR irradiation was performed in the +NIR group and +NIR+MF group for 14 days. Mice of these two groups were observed for another 14-day recovery and then sacrificed. Frozen sections were generated from the tumor tissues and imaged with a confocal microscope with a 980-nm NIR laser connected with fiber optics.

In addition, major tissue and blood samples were collected for histology analysis and blood biochemistry testing, respectively. Serum was collected by centrifuging the blood at 3,000 rpm for 10 min. Liver function was evaluated by assessing the levels of alanine aminotransferase (ALT) (in ESI), aspartate aminotransferase (AST) (in ESI), alkaline phosphatase (ALP), and total bilirubin (TBIL) in the serum. Blood urea nitrogen (UREA) and serum creatinine (CREA) (in ESI) were evaluated to determine nephrotoxicity. The biochemical parameters were determined according to the methods described in the references using commercial kits (Nanjing JianchengBioeng Inst., China). All histological tests were performed using standard laboratory procedures. The tissues were fixed with 4% (v/v) formalin, embedded in a paraffin block, sliced into 5-μm thick sections and placed onto glass slides. After hematoxylin-eosin (H&E) staining, the slides were examined by a pathologist using an optical microscope (Nikon U-III Multi-points Sensor System, USA).

Statistical analysis

The results were expressed as the mean ± standard deviation (SD). Comparisons among the groups were evaluated by *t*-test (two variables) or ANOVA (multiple variables) followed by the Student-Newman-Keuls test. A value of $p < 0.05$ was considered statistically significant.

Abbreviations

ALP: alkaline phosphatase; ALT: alanine aminotransferase; AST: aspartate aminotransferase; CREA: serum creatinine; CW: continuous wave; DA:

2,4-dihydroxybenzoic acid; DMEM: Dulbecco's modified Eagle's medium; EDS: energy dispersive spectroscopy; FBS: fetal bovine serum; FeCUPs: amphiphilic poly(ethylene glycol)-coated FeCU; FeP: the precursor of FeC; FeCU: the UCNP-loaded FeC; FTIR: Fourier transform infrared; H&E: hematoxylin-eosin; HMT: hexamethylenetetranrine; HRTEM: high-resolution transmission electron microscopy; ICP-AES: inductively coupled plasma-atomic emission spectrometry; Mn: number-average molecular weight; MRI: magnetic resonance imaging; NIR: near infrared; FeC: the Fe_3O_4-loaded hollow carbon sphere; OA: oleic acid; ODE: 1-octadecene; PTT: photothermal therapy; SD: standard deviation; STEM-HAADF: high-angle annular dark-field scanning transmission electron microscopy; TBIL: total bilirubin; TEA: trimethylamine; TEM: transmission electron microscope; UCL: upconversion luminescence; UCNPs: upconversion nanoparticles; UREA: blood urea nitrogen

Acknowledgements

We are grateful for the financial support from the National Natural Science Foundation of China (Grant Nos. 21571125, 31671011, 11575107), Medical Research Project of Jiangsu Provincial Commission of Health and Family Planning (NO. Z201624), and the National Key R&D Program of China (No. 2016YFE0114800).

Supplementary Material

Supplementary figures.
http://www.thno.org/v09p0608s1.pdf

Competing Interests

The authors have declared that no competing interest exists.

References

1. Organization WH. World cancer day: global action to avert 8 million cancer-related deaths by 2015. Indian Journal of Medical Sciences. 2006; 60: 85-6.
2. Zhao X, Yang CX, Chen LG, Yan XP. Dual-stimuli responsive and reversibly activatable theranostic nanoprobe for precision tumor-targeting and fluorescence-guided photothermal therapy. Nat Commun. 2017; 8: 14998.
3. Li Z, Liu J, Hu Y, et al. Biocompatible PEGylated bismuth nanocrystals: "all-in-one" theranostic agent with triple-modal imaging and efficient *in vivo* photothermal ablation of tumors. Biomaterials. 2017; 141: 284-95.
4. Zeng L, Luo L, Pan Y, Luo S, Lu G, Wu A. *In vivo* targeted magnetic resonance imaging and visualized photodynamic therapy in deep-tissue cancers using folic acid-functionalized superparamagnetic-upconversion nanocomposites. Nanoscale. 2015; 7: 8946-54.
5. Xu H, Cheng L, Wang C, Ma X, Li Y, Liu Z. Polymer encapsulated upconversion nanoparticle/iron oxide nanocomposites for multimodal imaging and magnetic targeted drug delivery. Biomaterials. 2011; 32: 9364-73.
6. Chen H, Qi B, Moore T, et al. Synthesis of brightly PEGylated luminescent magnetic upconversion nanophosphors for deep tissue and dual MRI imaging. Small. 2014; 10: 160-8.
7. Dave SR, Gao X. Monodisperse magnetic nanoparticles for biodetection, imaging, and drug delivery: a versatile and evolving technology. Wiley Interdiscip Rev Nanomed Nanobiotechnol. 2009; 1: 583-609.
8. Gao M, Yu F, Lv C, Choo J, Chen L. Fluorescent chemical probes for accurate tumor diagnosis and targeting therapy. Chem Soc Rev. 2017; 46: 2237-71.
9. Wu X, Chen G, Shen J, Li Z, Zhang Y, Han G. Upconversion nanoparticles: a versatile solution to multiscale biological imaging. Bioconjug Chem. 2015; 26: 166-75.
10. Hilderbrand SA, Weissleder R. Near-infrared fluorescence: application to *in vivo* molecular imaging. Curr Opin Chem Biol. 2010; 14: 71-9.
11. Boyer JC, Cuccia LA, Capobianco JA. Synthesis of colloidal upconverting NaYF4: Er3+/Yb3+ and Tm3+/Yb3+ monodisperse nanocrystals. Nano Lett. 2007; 7: 847-52.
12. Zhou J, Chen G, Wu E, et al. Ultrasensitive polarized up-conversion of Tm3+–Yb3+ doped β-NaYF4 single nanorod. Nano Lett. 2013; 13: 2241-6.
13. Chen G, Ohulchanskyy TY, Kumar R, Ågren H, Prasad PN. Ultrasmall monodisperse NaYF4:Yb3+/Tm3+ nanocrystals with enhanced near-infrared to near-infrared upconversion photoluminescence. ACS Nano. 2010; 4: 3163-8.
14. Liu Q, Sun Y, Yang T, Feng W, Li C, Li F. Sub-10 nm hexagonal lanthanide-doped NaLuF4 upconversion nanocrystals for sensitive bioimaging *in vivo*. J Am Chem Soc. 2011; 133: 17122-5.
15. Zhu X, Feng W, Chang J, et al. Temperature-feedback upconversion nanocomposite for accurate photothermal therapy at facile temperature. Nat Commun. 2016; 7: 10437.
16. Yang D, Yang G, Yang P, et al. Assembly of Au plasmonic photothermal agent and iron oxide nanoparticles on ultrathin black phosphorus for targeted photothermal and photodynamic cancer therapy. Adv Funct Mater. 2017; 27: 1700371.
17. Yang K, Zhang S, Zhang G, Sun X, Lee ST, Liu Z. Graphene in mice: ultrahigh *in vivo* tumor uptake and efficient photothermal therapy. Nano Lett. 2010; 10: 3318-23.
18. Espinosa A, Di Corato R, Kolosnjaj-Tabi J, Flaud P, Pellegrino T, Wilhelm C. Duality of iron oxide nanoparticles in cancer therapy: amplification of heating efficiency by magnetic hyperthermia and photothermal bimodal treatment. ACS Nano. 2016; 10: 2436-46.
19. Tay ZW, Chandrasekharan P, Chiu-Lam A, et al. Magnetic particle imaging-guided heating *in vivo* using gradient fields for arbitrary localization of magnetic hyperthermia therapy. ACS Nano. 2018; 12: 3699-713.
20. Chen YW, Su YL, Hu SH, Chen SY. Functionalized graphene nanocomposites for enhancing photothermal therapy in tumor treatment. Adv Drug Deliv Rev. 2016; 105: 190-204.
21. Biju V. Chemical modifications and bioconjugate reactions of nanomaterials for sensing, imaging, drug delivery and therapy. Chem Soc Rev. 2014; 43: 744-64.
22. Liu JN, Shi JL, Bu WB. Chapter 10 near infrared-triggered synergetic cancer therapy using multifunctional nanotheranostics. In: Zhang F, Ed. Near-Infrared Nanomaterials: Preparation, Bioimaging and Therapy Applications. UK: The Royal Society of Chemistry; 2016: 322-54.
23. Wang K, Huang L, Razzaque S, Jin S, Tan B. Fabrication of hollow microporous carbon spheres from hyper-crosslinked microporous polymers. Small. 2016; 12: 3134-42.
24. Yang HW, Liu HL, Li ML, et al. Magnetic gold-nanorod/ PNIPAAmMA nanoparticles for dual magnetic resonance and photoacoustic imaging and targeted photothermal therapy. Biomaterials. 2013; 34: 5651-60.
25. Cheng L, Yang K, Li Y, et al. Facile preparation of multifunctional upconversion nanoprobes for multimodal imaging and dual-targeted photothermal therapy. Angew Chem Int Ed Engl. 2011; 50: 7385-90.
26. Chen G, Song J, Zhang H, et al. Pd nanoparticles encapsulated in magnetic carbon nanocages: an efficient nanoenzyme for the selective detection and multicolor imaging of cancer cells. Nanoscale. 2015; 7: 14393-400.
27. Zhang F, Braun GB, Pallaoro A, et al. Mesoporous multifunctional upconversion luminescent and magnetic "nanorattle" materials for targeted chemotherapy. Nano Lett. 2012; 12: 61-7.
28. Yao L, Zhou J, Liu J, Feng W, Li F. Iridium-complex-modified upconversion nanophosphors for effective LRET detection of cyanide anions in pure water. Adv Funct Mater. 2012; 22: 2667-72.
29. Li L, Sun W, Zhong J, et al. Multistage nanovehicle delivery system based on stepwise size reduction and charge reversal for programmed nuclear targeting of systemically administered anticancer drugs. Adv Funct Mater. 2015; 25: 4101-13.
30. Liu R, Xiao W, Hu C, Xie R, Gao H. Theranostic size-reducible and no donor conjugated gold nanocluster fabricated hyaluronic acid nanoparticle with optimal size for combinational treatment of breast cancer and lung metastasis. J Control Release. 2018; 278: 127-39.
31. Na JH, Lee S, Koo H, et al. T1-weighted MR imaging of liver tumor by gadolinium-encapsulated glycol chitosan nanoparticles without non-specific toxicity in normal tissues. Nanoscale. 2016; 8: 9736-45.
32. Cui S, Wei J, Xiaosong, Xu S, Sun Z, Zhu R. Microscopic expression of the surface tension of nano-scale cylindrical liquid and applicability of the laplace equation. J Comput Theor Nanosci. 2015; 12: 189-93.
33. Flauraud V, Mastrangeli M, Bernasconi GD, et al. Nanoscale topographical control of capillary assembly of nanoparticles. Nat Nanotechnol. 2017; 12: 73-80.
34. Lee M, Kim B, Kim J, Jhe W. Noncontact friction via capillary shear interaction at nanoscale. Nat Commun. 2015; 6: 7359.
35. de Boer MP, Knapp JA, Michalske TA, Srinivasan U, Maboudian R. Adhesion hysteresis of silane coated microcantilevers. Acta Mater. 2000; 48: 4531-41.
36. Saldías C, Méndez-López M, Saavedra-Torres M, et al. Interfacial behavior of PAMAM-PCL dendrimers and in situ spontaneous formation of gold

nanoparticles at the toluene-water and air-water interfaces: experimental and theoretical studies. Eur Polym J. 2016; 84: 188-204.
37. Yuan Y, Li X, Tu J. The effects of nanoparticles on the lift force and drag force on bubbles in nanofluids: a two-fluid model study. Int J Therm Sci. 2017; 119: 1-8.
38. Sakho EHM, Allahyari E, Oluwafemi OS, Thomas S, Kalarikkal N. Chapter 2 - dynamic light scattering (DLS). In: Thomas S, Thomas R, Zachariah AK, Mishra RK, Eds. Thermal and Rheological Measurement Techniques for Nanomaterials Characterization. Amsterdam, NL: Elsevier; 2017: 37-49.
39. Moore J, Cerasoli E. Particle light scattering methods and applications. In: Lindon JC, Tranter GE, Koppenaal DW, Ed. Encyclopedia of Spectroscopy and Spectrometry. Oxford, UK: Academic Press; 2017: 543-53.
40. Xu M, Yin B, Li C, Yao P. Fe3O4 and paclitaxel loaded emulsion with charge-conversional surface for tumor MRI and therapy. RSC Adv. 2015; 5: 40831-9.
41. Pereira C, Pereira AM, Rocha M, Freire C, Geraldes CFGC. Architectured design of superparamagnetic Fe3O4 nanoparticles for application as MRI contrast agents: mastering size and magnetism for enhanced relaxivity. J Mater Chem B. 2015; 3: 6261-73.
42. Cheong S, Ferguson P, Feindel KW, et al. Simple synthesis and functionalization of iron nanoparticles for magnetic resonance imaging. Angew Chem Int Ed Engl. 2011; 50: 4206-9.
43. Wu T, Pan H, Chen R, et al. Effect of solution pH value changes on fluorescence intensity of magnetic-luminescent Fe3O4@Gd2O3:Eu3+ nanoparticles. Journal of Rare Earths. 2016; 34: 71-6.
44. Rosensweig RE. Heating magnetic fluid with alternating magnetic field. J Magn Magn Mater. 2002; 252: 370-4.
45. Chen H, Shao L, Ming T, et al. Understanding the photothermal conversion efficiency of gold nanocrystals. Small. 2010; 6: 2272-80.
46. Ge X, Song ZM, Sun L, et al. Lanthanide (Gd3+ and Yb3+) functionalized gold nanoparticles for *in vivo* imaging and therapy. Biomaterials. 2016; 108: 35-43.
47. Wang X, Cao D, Tang X, et al. Coating carbon nanosphere with patchy gold for production of highly efficient photothermal agent. ACS Appl Mater Interfaces. 2016; 8: 19321-32.
48. Zhang L, Chen L, Liu J, Fang X, Zhang Z. Effect of morphology of carbon nanomaterials on thermo-physical characteristics, optical properties and photo-thermal conversion performance of nanofluids. Renew Energy. 2016; 99: 888-97.
49. Saba TM. Physiology and physiopathology of the reticuloendothelial system. Arch Intern Med. 1970; 126: 1031-52.
50. Kabel AM. Tumor markers of breast cancer: new prospectives. J Oncol Sci. 2017; 3: 5-11.
51. Park J, An K, Hwang Y, et al. Ultra-large-scale syntheses of monodisperse nanocrystals. Nat Mater. 2004; 3: 891-5.
52. Sun Q, Guo CZ, Wang GH, Li WC, Bongard H-J, Lu AH. Fabrication of magnetic yolk-shell nanocatalysts with spatially resolved functionalities and high activity for nitrobenzene hydrogenation. Chemistry. 2013; 19: 6217-20.
53. Prencipe G, Tabakman SM, Welsher K, et al. PEG branched polymer for functionalization of nanomaterials with ultralong blood circulation. J Am Chem Soc. 2009; 131: 4783-7.
54. Wei R, Wei Z, Sun L, et al. Nile red derivative-modified nanostructure for upconversion luminescence sensing and intracellular detection of Fe3+ and MR imaging. ACS Appl Mater Interfaces. 2016; 8: 400-10.
55. Zou X, Liu Y, Zhu X, et al. An Nd3+-sensitized upconversion nanophosphor modified with a cyanine dye for the ratiometric upconversion luminescence bioimaging of hypochlorite. Nanoscale. 2015; 7: 4105-13.